

5G NTN Primary Synchronization Signal: An Improved Detector for Handheld Devices

*Original*

5G NTN Primary Synchronization Signal: An Improved Detector for Handheld Devices / Tuninato, Riccardo; Garelo, Roberto. - In: IEEE OPEN JOURNAL OF THE COMMUNICATIONS SOCIETY. - ISSN 2644-125X. - ELETTRONICO. - 5:(2024), pp. 3792-3803. [10.1109/ojcoms.2024.3416554]

*Availability:*

This version is available at: 11583/2990042 since: 2024-07-01T10:00:21Z

*Publisher:*

IEEE

*Published*

DOI:10.1109/ojcoms.2024.3416554

*Terms of use:*

This article is made available under terms and conditions as specified in the corresponding bibliographic description in the repository

*Publisher copyright*

(Article begins on next page)

# 5G NTN Primary Synchronization Signal: An Improved Detector for Handheld Devices

**RICCARDO TUNINATO<sup>ID</sup>** (Graduate Student Member, IEEE),  
**AND ROBERTO GARELLO<sup>ID</sup>** (Senior Member, IEEE)

Department of Electronics and Telecommunications, Politecnico di Torino, 10129 Turin, Italy

CORRESPONDING AUTHOR: R. GARELLO (e-mail: roberto.garello@polito.it)

**ABSTRACT** We consider a Low Earth Orbit (LEO) satellite hosting a 5G base station transmitting to a handheld device in L-band or S-band. This link is critical because it is characterized by a very low Signal-to-Noise Ratio and significant Residual Frequency Offset (RFO) due to imperfect Doppler compensation. Usual methods adopted to detect the Primary Synchronization Signal (PSS) during Cell Search of terrestrial networks may fail in these conditions. In this paper we present an improved method for PSS detection, working in the frequency domain and exploiting the peculiar structure of the 5G PSS. We derive the exact analytical model, taking into account the Orthogonal Frequency Division Multiplexing (OFDM) InterCarrier Interference (ICI) and we obtain the corresponding optimal statistical test. We present a number of results showing that the new detector achieves significant performance improvements for realistic 5G Non-Terrestrial Network (NTN) scenarios.

**INDEX TERMS** Non-terrestrial networks, 5G new radio, cell search, primary synchronization signal, frame synchronization.

## I. INTRODUCTION

THE GROWING interest in 5G NTN stems from the need to extend the capabilities of the fifth generation of wireless mobile networks beyond the terrestrial boundaries. While 5G has already brought about significant improvements in terms of speed, capacity, and latency on the ground, it faces limitations when it comes to providing seamless connectivity in remote, rural, or hard-to-reach areas. NTN offers a promising solution by harnessing the power of LEO satellite communication to ensure connectivity in previously underserved regions. This technology not only promises to bridge the digital divide, but also opens new avenues for applications in disaster management, precision agriculture, environmental monitoring, and more. The intersection of 5G and NTN represents an exciting frontier in the world of telecommunications and is poised to revolutionize the way we stay connected.

3GPP has studied two frequency ranges for NTN, corresponding to two types of devices:

- L-band (1.6 GHz) and S-band (2 GHz) for handheld devices (regular smartphones, 23 dBm transmitted power).

- Ka-band (20/30 GHz) for high-gain devices with directive antennas (Fixed Wireless Access and IoT Gateways).

For handheld devices, the link budget is tight but still good enough for outdoor use. Anyway, the same techniques that work for terrestrial access must be modified when the NTN link is considered. In addition to the very low Signal-to-Noise Ratio (SNR) due to the long-range (600 km of altitude or more) and non-directive antennas, the main problem is the RFO. In fact, LEO satellites are characterized by large values of Doppler shift and Doppler rate. Even though devices can rely on a map of satellite ephemerides and compute a Doppler estimation, imperfect estimation and Doppler rate cause the presence of a significant RFO. These two impairments have a very strong impact on 5G initial access procedures.

In 5G New Radio (NR) the initial access is divided into the Synchronization Procedure and the Random Access procedure, sequentially organised. The synchronization procedure aims to correctly align the handheld device to the time and frequency grid reference and to provide key information on the Base Station, and it is often referred to as Cell Search (CS).

5G NR Cell Search is based on the Synchronization Signal Block (SSB), which contains both the Primary and Secondary Synchronization Signals (PSS and SSS), plus the Physical Broadcast Channel (PBCH), with its associated Demodulation Reference Signal (DMRS). While synchronization signals are generated as pseudo-random noise sequences, the physical channel contains polar encoded data [1].

The PSS must be decoded first because it contains a key portion of the cell's Physical Cell Identity (PCID). In terrestrial scenarios, frame synchronization is usually realized via standard non-coherent correlation. The performance of this method significantly degrades in the presence of an RFO due to imperfect Doppler compensation. In 5G NTN, the idea is to reuse the same SSB structure as NR [2].

In this paper, we present a new detector that, by working in the frequency domain, exploits the peculiar structure of the 5G PSS and a precise model of the frequency offset (FO) effect, and is able to achieve significant performance improvements in typical 5G NTN scenarios.

#### A. PREVIOUS LITERATURE

The literature on 5G terrestrial Cell Search is quite extensive. A tutorial on CS evolution in 3G, 4G and 5G can be found in [3] and [4] provides a comprehensive analysis of 5G synchronization. In [5] the author analysed the 5G time and frequency accuracy requirements of the user alignment with the network resource grid. Authors in [6] introduced a novel method for offloading the UE computational requirements for CS to the BS.

Different works addressed 5G terrestrial PSS detection in the literature. Yuexia He et al. [7] analyzed different PSS design variants and evaluated their performance for different subcarrier spacings (SCS). In [8] and [9], different correlation-based techniques have been studied for PSS detection, paying attention to the FO impact, whereas the novel technique developed in [10] aims at improving the detection with a refinement step via the triple autocorrelation property of the m-sequences [11]. In [12] another version of the PSS detection is developed based on the Cyclic Prefix (CP) autocorrelation, whereas in [13] a reduced-complexity approach is proposed, at the cost of some performance losses. Authors in [14] adopted a Convolutional Neural Network (CNN) solution to address the synchronization and authors in [15] proposed an optimization algorithm for the hardware resources consumption of PSS detection.

As for 5G satellite PSS detection, an interesting analysis was presented by Cassiau et al. in [16]. Authors adopted a PSS detection approach in the frequency domain, after time synchronization through CP, in a study of the implementation of 5G physical layer for satellite transmissions. The standard non-coherent cross-correlation was considered for PSS detection. Synchronization for initial FO compensation in NTN has been studied in [17], to deal with very large Doppler shifts.

Some studies have been conducted also for the 3GPP working groups. As an example, in [18] ZTE provided results for SSB detection. The implementation details are not disclosed, but they reported that the large initial FO is treated with multi-branch detection (the detection is repeated, or parallelized, for different possible values of large FO, i.e., exceeding the subcarrier size). Huawei and HiSilicon, in [19], reported results for PSS detection, where they exploited two receiving antennas and time accumulation with different periodicity. However, in this work we focus on single-shot PSS detection.

Finally, a number of papers written by Chiani et al. for frame synchronization studied the optimal estimator under given circumstances: [20] for Additive White Gaussian Noise (AWGN) channel, [21] in the presence of phase offset, and [22] for a pattern surrounded by  $M$ -PSK symbols.

To summarize, even if a relevant number of works dealt with synchronization in terrestrial 5G, only a few numbers investigated it in NTN, that also requires a different channel model than the terrestrial one. Moreover, they did not investigate the optimum metric for the particular SSB structure.

#### B. CONTRIBUTIONS

In this paper we present an enhanced PSS detector for 5G NTN reception on handheld devices in L-band or S-band. This scenario is characterized by low SNR and RFO due to imperfect Doppler compensation. The new method works in the frequency domain and exploits the knowledge of the SSB actual structure.

The new detector is derived by taking into account:

- the exact analytical model of the ICI term due to the RFO impact on OFDM sub-carriers;
- the M-PSK nature of the SSS and PBCH symbols surrounding the PSS;
- the extended pattern including the zero guard band that encompasses the PSS sequence.

The new detector is then analyzed under different NTN scenarios including both the AWGN and the Land Mobile Satellite (LMS) channel model, and compared against traditional terrestrial solutions. Results show a significant performance improvement with respect to usual detection techniques for the SNR and RFO ranges typical of NTN handheld solutions.

#### C. ORGANIZATION

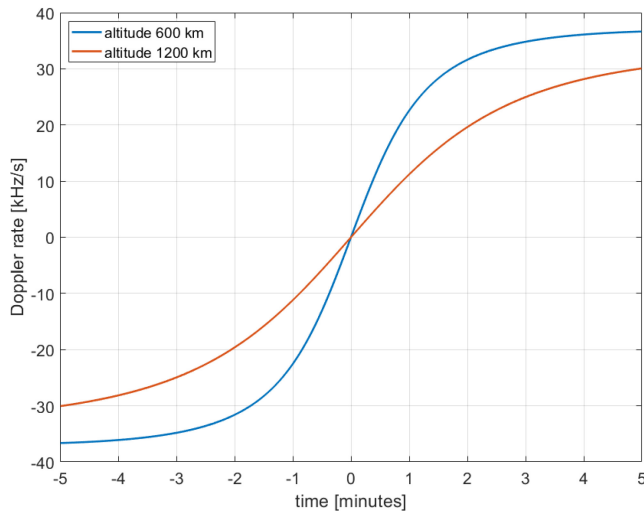
The paper is organized as follows. Section II introduces the 5G NTN scenario under analysis and contains a detailed description of the SSB and PSS. In Section III we present the derivation of the new PSS detector. Section IV describes the LMS channel model. In Section V the simulation results for different NTN scenarios are reported and discussed. Finally, the conclusions are outlined in Section VI.

**TABLE 1.** Path loss for different altitudes and different bands of NTN satellites. The satellite elevation is fixed at 90°.

	L-band 1.6 GHz	S-band 2 GHz	Ka-band 20 GHz
$h$ [km]	Path loss [dB]	Path loss [dB]	Path loss [dB]
600	152	154	174
1200	158	160	180

**TABLE 2.** Doppler shift and doppler rate (maximum) for different altitudes and different bands of NTN satellites.

	L-band 1.6 GHz	S-band 2 GHz	Ka-band 20 GHz
$h$ [km]	Doppler shift/rate [kHz]/[kHz/s]	Doppler shift/rate [kHz]/[kHz/s]	Doppler shift/rate [kHz]/[kHz/s]
600	36 / 0.46	46 / 0.58	460 / 5.8
1200	30 / 0.20	38 / 0.25	380 / 2.5

**FIGURE 1.** Doppler shift for L-band.

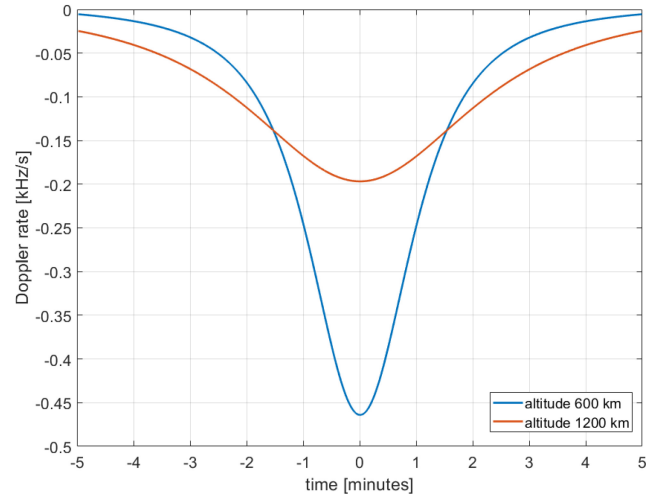
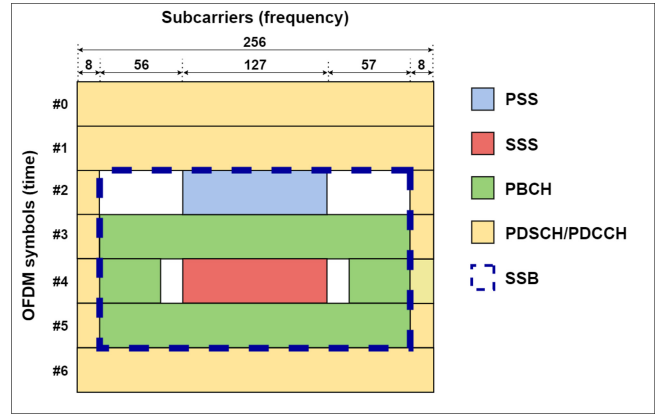
## II. 5G NTN

3GPP has issued Release 17 of the 5G NR standard, encompassing non-terrestrial networks (NTN) [23], broadening the study on NR support for NTN in Release 15 [24]. Two types of devices are planned, operating on different bands:

- Handheld devices (regular smartphones, 23 dBm transmitted power), operating on L-band (1.6 GHz) and S-band (2 GHz). 3GPP categorizes these bands as L-band n255 and S-band n256, plus a mixed L/S-band n254 [25].
- High-gain devices with directive antennas (Fixed Wireless Access and IoT Gateways), operating on Ka-band (20/30 GHz).

In this paper, we focus on this use case:

- NTN configuration: Direct Access
- NTN service: Enhanced Mobile Broadband
- Beam/cell type: Earth fixed
- Payload: Regenerative
- Orbit: LEO (600/1200 km)

**FIGURE 2.** Doppler rate for L-band.**FIGURE 3.** SSB allocation in the resource grid.

- NTN terminal condition: outdoor, Line-of-Sight (LOS).

Some examples of the corresponding path loss for nominal altitudes  $h$  for the different bands are reported in Table 1, computed via Free Space Path Loss (FSPL) criteria in dB, as in Eq. (6).6-2 of [24]. Some examples of the expected Doppler shift and Doppler rate values are reported in Table 2, Figure 1 and Figure 2, characterizing the Doppler shift and rate for LEO satellites as in [26].

### A. 5G SYNCHRONIZATION SIGNAL BLOCK

In 5G, the Synchronization Signal Block (SSB) assembles PSS/SSS/PBCH into a single structure, periodically transmitted on the downlink by each NR cell to perform the synchronization procedure [27]. As shown in Figure 3, the SSB occupies a total amount of 960 resource elements in the OFDM grid: 4 OFDM symbols in the time domain and 240 contiguous subcarriers (20 Resource Blocks) in the frequency domain, for each OFDM symbol. [28, Table 7.4.3.1-1] describes in detail the organization of the resources of the SSB. The actual bandwidth and the time duration of the SS-Block depends on the numerology  $\mu$  adopted by the network since the SCS is  $\Delta f = 15 \cdot 2^\mu$  kHz.

Different numerologies are possible for 5G NTN deployment for frequency bands below 6 GHz, i.e.,  $\mu = 0$  ( $\Delta f = 15$  kHz),  $\mu = 1$  ( $\Delta f = 30$  kHz),  $\mu = 2$  ( $\Delta f = 60$  kHz) and  $\mu = 3$  ( $\Delta f = 120$  kHz).

In this paper, we take as a reference a 5G NTN deployment at L-band, with numerology  $\mu = 1$ . The SCS is 30 kHz and the OFDM symbol time length is  $T_s = 1/\Delta f = 33.33$   $\mu$ s. Thus, the SSB occupies 7.2 MHz and lasts 133.33  $\mu$ s. In [24], the use of both numerology 0 and 1 are considered for below 6 GHz bands for link level simulations. However, a numerology of 2 is also suggested for increased SCS and thus higher robustness against the Doppler shift. The chosen numerology must respect the available bandwidth, and bandwidths of 5, 10 and 15 MHz are specified at the moment for S-/L-band [25]. A SCS of 15 kHz must be applied if the Downlink bandwidth is less than the SSB band, as in the case of 5 MHz bandwidth. The periodicity of the SSB is flexible in 5G NR, but it is common to adopt an interval of 20 ms. In the case of multiple beams, up to 8 SSBs can be transmitted in a 5 ms interval, and each SSB is assigned to one beam. As shown in Figure 3, the SSB is surrounded by PDSCH/PDCCH (Primary Downlink Shared Channel/Primary Downlink Control Channel) data or control symbols [29].

### B. PRIMARY SYNCHRONIZATION SIGNAL

PSS and SSS signals permit the determination of the Physical Cell Identity (PCID) of the cell. In 5G NR the PCID  $N_{ID}^{cell}$  can assume 1008 different values and it is given by

$$N_{ID}^{cell} = 3N_{ID}^{(1)} + N_{ID}^{(2)} \quad (1)$$

where the cell identity group index  $N_{ID}^{(1)} (\in \{0, 1, \dots, 335\})$ , is carried by the SSS and the sector identity  $N_{ID}^{(2)} (\in \{0, 1, 2\})$  is carried by the PSS [28]. Other than providing the  $N_{ID}^{(2)}$  value, the PSS is used to acquire the initial symbol alignment and the coarse frequency correction. The latter is fundamental since the Doppler and UE oscillator inaccuracy produces a mismatch with the carrier frequency of the reference system.

NR PSS is generated in the frequency domain as a BPSK maximal-length sequence (m-sequence) of 127 symbols, thus occupying 127 subcarriers, out of the 240 of the SS-Block frequency dimension. Differently from the SSS, all the remaining SSB subcarriers in the same OFDM symbol are reserved as guard bands, i.e., they are set to zero. There are three different possible PSS sequences  $\mathbf{d}^{(k)}$  depending on the three different values that  $k = N_{ID}^{(2)}$  can assume [28]

$$d_n^{(k)} = 1 - 2x_m \quad 0 \leq n \leq 127 \quad (2)$$

$$m = (n + 43k) \mod 127 \quad (3)$$

where the polynomial  $x(i)$  is given by the recursive formula:

$$x_{i+7} = (x_{i+4} + x_i) \mod 2. \quad (4)$$

Then, the three PSS sequences correspond to three cyclic shifts of one m-sequence, generated by a Linear Feedback

Shift Register with seven cells and generator polynomial  $1 + D^4 + D^7$ .

Note that also in LTE there were 3 possible PSSs, but generated as Zadoff-Chu sequences with a length of 62. The switch to m-sequences was motivated by the time and frequency offset ambiguity affecting Zadoff-Chu sequences: the correlation function outputs undesired periodical peaks along the frequency axis, and side peaks along the time axis [30]. 5G PSS allows the estimation of the FO in one-shot, while in LTE the PSS detection would provide a set of candidates, equally spaced in frequency. Doubling the sequence length results also in a 3 dB larger processing gain, due to the higher peak with respect to the correlation noise floor.

For the application of our detector, it is important to note that the SSS symbols (corresponding to Gold sequences) are mapped into 2-PSK symbols, while the PBCH symbols (that occupy most of the SSB) are mapped into 4-PSK symbols [27].

### C. INITIAL SYNCHRONIZATION

Some steps must be performed before starting PSS synchronization.

As a realistic assumption for 5G NTN operations, we suppose that the handheld device knows the satellite ephemerides and computes a first Doppler estimation and pre-compensation [24].

The second step is numerology detection. We know that different numerologies are planned for 5G NTN. As mentioned in the previous section, there are different possible values for numerology at L-band, from  $\mu = 0$  to  $\mu = 3$ . The numerology detection can be performed by running four autocorrelation computations in parallel, one for each numerology.

The third step is the alignment to the time grid. As explained in [16], a time-domain OFDM symbol synchronization is performed by computing the 1-bit autocorrelations on Cyclic Prefix-length windows. Since the Cyclic Prefix length decreases with the numerology, consecutive autocorrelations must be aggregated to achieve the same accuracy for each  $\mu$ , while remaining inside a one-frame duration.

The fourth step is a first estimation of the Carrier Frequency Offset (CFO). This can be done by analyzing the autocorrelation peak and deriving an estimation of the CFO fractional part, which is then digitally compensated in the time domain.

At this point, we can start the PSS detection in the presence of an RFO in the frequency domain as explained in the next sections.

### III. THE NEW IMPROVED PSS DETECTOR

In this section we analytically derive an enhanced detector for the PSS. It is based on three steps:

- The first is to precisely derive the model that accounts for the ICI caused by the loss of orthogonality of the OFDM subcarriers due to the RFO.

- The second is to consider the optimal statistical test for this model.
- The third is to adapt it to take into account the actual structure of the SSB.

The three steps are addressed in the following.

#### A. EXACT MODEL FOR OFDM RECEIVED SYMBOLS IN PRESENCE OF FREQUENCY OFFSET

Let us denote by  $\mathbf{X} = (X_0, \dots, X_m, \dots, X_{N-1})$  the vector of  $N$  transmitted PSK/QAM complex symbols before OFDM modulation (frequency domain).

The vector of  $N$  transmitted complex samples after OFDM modulation (time domain) is  $\mathbf{x} = (x_0, \dots, x_n, \dots, x_{N-1})$ , where

$$x_n = \frac{1}{N} \sum_{m=0}^{N-1} X_m e^{j2\pi nm/N}.$$

The vector of  $N$  received complex samples (time domain) in case of line-of-sight link and FO  $\psi$  is  $\mathbf{y} = (y_0, \dots, y_n, \dots, y_{N-1})$ , and its  $n$ -th sample  $y_n$  is given by

$$y_n = \frac{1}{N} \sum_{m=0}^{N-1} h_n X_m e^{j2\pi n(m+\Delta F)/N} + w_n \quad (5)$$

where  $\Delta F = \psi/\Delta f$  is the FO normalized by the SCS,  $\mathbf{h} = (h_0, \dots, h_n, \dots, h_{N-1})$  is the vector containing the channel realizations in time, and  $\mathbf{w} = (w_0, \dots, w_n, \dots, w_N)$  is the vector containing the complex Gaussian noise samples with zero mean and  $\sigma^2$  variance. The vector of  $N$  received complex symbols after OFDM demodulation (frequency domain) is  $\mathbf{Y} = (Y_0, \dots, Y_m, \dots, Y_{N-1})$ , where

$$Y_m = \sum_{n=0}^{N-1} y_n e^{-j2\pi nm/N}.$$

By substituting the expression from Equation (4) and solving the finite geometric series we obtain

$$Y_m = X_m \eta_{m,m} + \sum_{i \neq m} X_i \eta_{i,m} + W_m \quad (6)$$

where

$$\eta_{m,m} = \frac{\sin(\pi \Delta F)}{N \sin(\pi \Delta F/N)} e^{j\pi \Delta F(N-1)/N} H_m$$

and

$$\eta_{i,m} = \frac{\sin(\pi \Delta F)}{N \sin(\pi(i-m+\Delta F)/N)} \times e^{j\pi \Delta F(N-1)/N} e^{-j\pi(i-m)/N} H_i \text{ for } i \neq m.$$

The complex symbol  $Y_m$  received on subcarrier number  $m$  is made by three components. The first is the transmitted symbol  $X_m$  subject to a reduction of amplitude and a phase shift depending on the FO. The second term is the ICI caused by the other transmitted symbols  $X_i, i \neq m$ . The third term is the noise complex Gaussian term  $W_m$ , with zero mean and variance  $\sigma_w^2$ , resulting from the Discrete Fourier Transform

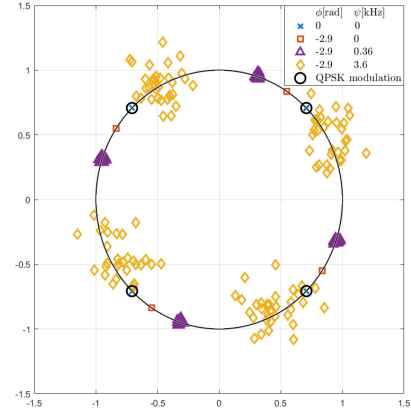


FIGURE 4. Scatter plot of the received QPSK symbols, SNR = 100 dB

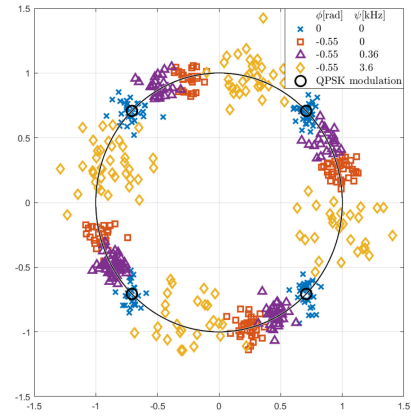


FIGURE 5. Scatter plot of the received QPSK symbols, SNR = 20 dB

(DFT) of the time domain  $\mathbf{w}$ . The first two terms are also affected by  $\mathbf{H} = (H_0, \dots, H_m, \dots, H_{N-1})$ , the vector containing the channel response after OFDM demodulation.

The effect of FO on QPSK received symbols can be seen in Figure 4 and Figure 5, which appears as an additional phase offset on the interested symbol, and as an additional noise given by the surrounding symbols. Of particular interest for our work is to analyze the impact of the FO (and thus, the ICI) on the detection procedure.

Let us focus on the second term of Equation (6), the ICI term:

$$W_{ICI,m} = \sum_{i \neq m} X_i \eta_{i,m}$$

$W_{ICI,m}$  is the sum of  $N - 1$  i.i.d. random variables  $X_k$  with  $k \in \{1, \dots, N\}, k \neq m$ , each multiplied by the factor  $\eta_{k,m}$ . For the Central Limit Theorem, it can be modelled as an additional Gaussian noise term [31], [32]. This can also be seen in Figure 6, where we performed a Quantile-Quantile test to compare the ICI term distribution against the standard normal distribution. The linearity of the quantile points suggests that the ICI term is approximately normally distributed.



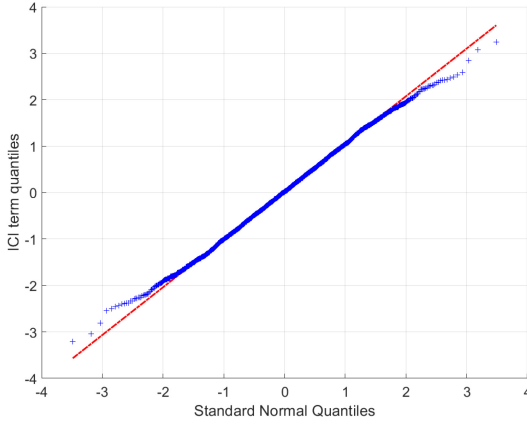


FIGURE 6. Quantile-Quantile test for the ICI term.

The variance  $\sigma_{\text{ICI}}^2$  is related to the FO  $\psi$  and SCS  $\Delta f$ , and can be computed as

$$\begin{aligned}\sigma_{\text{ICI}}^2 &= \mathbb{E}[|W_{\text{ICI}}|^2] = \mathbb{E}\left[\left|\sum_{\substack{k=1 \\ k \neq m}}^N X_k \eta_{k,m}\right|^2\right] = \\ &= \sum_{\substack{k=1 \\ k \neq m}}^N \mathbb{E}[|X_k|^2] \mathbb{E}[|\eta_{k,m}|^2] = E_s \sum_{\substack{k=1 \\ k \neq m}}^N \mathbb{E}[|\eta_{k,m}|^2] \\ &= E_s \frac{\sin^2(\pi \Delta F)}{N^2} \sum_{\substack{k'=-m \\ k' \neq 0}}^N \frac{1}{\sin^2(\pi(\Delta F + k')/N)} \\ &= \frac{\sin^2(\pi \Delta F)}{N^2} \sum_{\substack{k'=-m \\ k' \neq 0}}^N \frac{1}{\sin^2(\pi(\Delta F + k')/N)}\end{aligned}$$

where  $E_s = \mathbb{E}[|X_k|^2]$  is the PSK symbol energy, which is equal to 1 in our case.

Finally, we have modelled our received symbols as

$$Y_m = \alpha X_m e^{j\theta} + \hat{W}_m \quad (7)$$

where  $\theta$  is a phase offset caused by the FO and where  $\hat{W}_m = W_{\text{ICI},m} + W_m$  is the Gaussian noise term, with zero mean and variance  $\hat{\sigma}_w^2 = \sigma_w^2 + \sigma_{\text{ICI}}^2$ .

## B. FALSE ALARM AND MISSED DETECTION PROBABILITIES

Considering the PSS detection problem, the receiver must decide if the received vector  $\mathbf{Y} = (Y_0, \dots, Y_m, \dots, Y_{N-1})$  contains the synchronization symbols. Let us denote with  $D_m$  the transmitted symbol  $X_m$  when data is transmitted, and with  $P_m$  the transmitted symbol  $X_m$  when the synchronization pattern is transmitted:

$$X_m = \begin{cases} D_m & \text{if data symbol} \\ P_m & \text{if synchronization symbol} \end{cases} \quad (8)$$

The synchronization is performed by a detector, which chooses between two hypotheses:

$$\mathcal{H}_0 : Y_m = \alpha D_m e^{j\theta} + \hat{W}_m \quad \forall m \ 1 \leq m \leq N \quad (9)$$

$$\mathcal{H}_1 : Y_m = \alpha P_m e^{j\theta} + \hat{W}_m \quad \forall m \ 1 \leq m \leq N. \quad (10)$$

To evaluate the performance of the detector, the probability of missed detection  $\mathcal{P}_{\text{MD}}$  and the probability of false alarm  $\mathcal{P}_{\text{FA}}$  (or false positive) are used.  $\mathcal{P}_{\text{MD}}$  is the probability of deciding  $\mathcal{H}_0$  (decision  $\mathcal{D}_0$ ) when  $\mathcal{H}_1$  is true, i.e., the synchronization sequence is transmitted but not detected

$$\mathcal{P}_{\text{MD}} = \mathcal{P}(\mathcal{D}_0 | \mathcal{H}_1). \quad (11)$$

$\mathcal{P}_{\text{FA}}$  is the probability of deciding  $\mathcal{H}_1$  (decision  $\mathcal{D}_1$ ) when  $\mathcal{H}_0$  is true, i.e., the detector erroneously decides that the synchronization sequence is present

$$\mathcal{P}_{\text{FA}} = \mathcal{P}(\mathcal{D}_1 | \mathcal{H}_0). \quad (12)$$

## C. NON-COHERENT AND COHERENT CORRELATOR

Due to the presence of the random phase, the commonly deployed detectors are based on the non-coherent correlation function, which is the cross-correlation between the received sequence  $\mathbf{Y}$  and the local replica of the PSS  $\mathbf{P} = (P_1, \dots, P_m, \dots, P_N)$  by applying

$$\Gamma_{\text{NC}} = \left| \sum_{m=1}^N Y_m^* P_m \right| \stackrel{\mathcal{D}_1}{\leq} \lambda \quad (13)$$

In order to perform the detection,  $\Gamma_{\text{NC}}$  is compared to a certain threshold  $\lambda$ . If  $\Gamma_{\text{NC}}$  is below  $\lambda$ , the detector decides for  $\mathcal{H}_0$ , otherwise it decides for  $\mathcal{H}_1$ .

The coherent correlation is not usually adopted because it is highly sensitive to phase shifts. In case of a fixed phase shift, that can be compensated through previous knowledge of the channel, coherent detection can be implemented as

$$\Gamma_C^{(\text{corr})} = \sum_{m=1}^N Y_m^* e^{j\hat{\theta}} P_m \quad (14)$$

where  $\hat{\theta}$  is the phase offset estimation provided by any previous signal processing operation, supposing such operation is available.

## D. STATISTICAL TEST UNDER PHASE OFFSET

Given the analytical model of Equation (7) that we have derived in Section III-A, the received symbol is affected by (i) the phase offset induced by the FO, (ii) the extra-noise term due to OFDM ICI and (iii) is surrounded by adjacent SSB symbols that are QPSK modulated (as PBCH).

The optimal statistical test for this scenario was studied in [22], where the authors derived the optimal likelihood ratio

test for QPSK modulated signal under phase offset. The test is given by:

$$\Gamma_A = \left| \sum_{m=1}^N \tilde{Y}_m^* P_m \right| - \max_l \left[ \sum_{m=1}^N \frac{1}{2} \left| \left( \tilde{Y}_m^I - \tilde{Y}_m^Q \right) \cos \phi_l + \left( \tilde{Y}_m^I + \tilde{Y}_m^Q \right) \sin \phi_l \right| + \sum_{m=1}^N \frac{1}{2} \left| \left( \tilde{Y}_m^I + \tilde{Y}_m^Q \right) \cos \phi_l + \left( \tilde{Y}_m^Q - \tilde{Y}_m^I \right) \sin \phi_l \right| \right] \quad (16)$$

where  $Y_m = Y_m^I + j Y_m^Q$  is the  $m$ -th received complex sample composed by the real (in-phase) and imaginary (in-quadrature) parts, respectively, and  $\tilde{Y}_m = Y_m / \sigma_w^2$  is the normalization concerning the noise variance.  $\phi_l = l\pi/N_q$ , with  $l \in \{0, 1, \dots, N_q - 1\}$ , is the  $l$ -th phase offset to be taken into account. The accuracy, but also the complexity, of  $\Gamma_A$ , increases with  $N_q$ , the number of evenly distributed phase offsets to be tested. In our analysis, we have verified that  $N_q = 4$  provides a very good trade-off for the metric implementation.

#### E. IMPROVED STATISTICAL TEST FOR PSS DETECTION

In this section, we complete the derivation of the new test, taking into account the received signal model (7) and the SSB structure. Consider a local sequence as long as the SSB in the frequency domain, i.e.,  $N^{(\text{ext})} = 240$  symbols. The extended sequence  $P^{(\text{ext})}$  is generated as

$$\mathbf{P}^{(\text{ext})} = (\mathbf{Z}_1 \mathbf{P} \mathbf{Z}_2) \quad (17)$$

where  $\mathbf{Z}_1$  and  $\mathbf{Z}_2$  are all-zeros vectors of length  $N^{(1)} = 56$  and  $N^{(2)} = 57$ , respectively. In this way, we obtain the same sequence transmitted in the first SSB symbol, and  $\Gamma_A$  is computed considering not only the synchronization sequence length but the extended pattern. We will refer to the metric with the extended pattern as  $\Gamma_A^{(\text{ext})}$ . This allows us to obtain an additional gain because we consider the complete structure of the SSB symbols, increasing the metric range that exploits the presence of modulated data.

Then, we can adapt Equation (16), by taking into account the results of Section III-A on the ICI variance and the extended PSS pattern. Thus, the scaling of the

received samples must take into consideration the new noise definition:  $\hat{Y}_m = Y_m / \hat{\sigma}_w^2$ . The final statistical test is obtained in Equation (15), shown at the bottom of the page.

The concept of the extended pattern can also be applied to another version of the statistical test, derived in [20], [33], which is a further approximation that only applies a correction term to the non-coherent correlation, given by the effect of embedded data in the received signal. It provides a lower complexity solution, and the result is the following:

$$\Gamma_B^{(\text{ext})} = \left| \sum_{m=N^{(1)}+1}^{N^{(1)}+N} \hat{Y}_m^* P_m^{(\text{ext})} \right| - \sum_{m=1}^{N^{(\text{ext})}} |\hat{Y}_m|. \quad (18)$$

1) Computational complexity: The computational complexity of the non-coherent correlation depends on  $N$ , the length of the synchronization sequence, times a constant  $\alpha$  that results from the operations carried out for each sample of the synchronization sequence. Considering that these operations consist of a product and then a sum,  $\alpha$  is 2. This operation is repeated until the detection, thus for  $L$  iterations:

$$\text{Complexity } \Gamma_{\text{NC}} = (\alpha N) L = (2 \cdot 127)L = 254L. \quad (19)$$

The improved method we propose is an operation with complexity equal to that of the non-coherent correlation plus an additional term that depends on  $N^{(\text{ext})}$ , the length of the extended pattern, and  $\beta$ , corresponding to the set of operations carried out in the right-hand side of Equation (15). With  $N_q = 4$ , these operations become 6 sums and 2 products (as in Equation (14) of [22]), and then  $\beta$  can be seen as equal to 8. Even in this case, the variable is only the number of iterations required to reach the detection, denoted as  $L_1$ :

$$\text{Complexity } \Gamma_A^{(\text{ext})} = L_1 (\alpha N + \beta N^{(\text{ext})}) = 2174L_1 \quad (20)$$

In general, we can state that the improved technique requires more complexity for the higher number of operations (of about a factor 8), but does not impact the overall linearity of the detector. For what concerns our alternative detector  $\Gamma_B^{(\text{ext})}$ , it requires a complexity equal to that of the non-coherent correlation plus the complexity of the correction term. It requires the computation of the absolute value and

$$\begin{aligned} \Gamma_A^{(\text{ext})} &= \left| \sum_{m=1}^{N^{(\text{ext})}} \hat{Y}_m^* P_m^{(\text{ext})} \right| - \frac{1}{2} \max_l \left[ \sum_{m=1}^{N^{(\text{ext})}} \left| \left( \hat{Y}_m^I - \hat{Y}_m^Q \right) \cos \phi_l + \left( \hat{Y}_m^I + \hat{Y}_m^Q \right) \sin \phi_l \right| + \sum_{m=1}^{N^{(\text{ext})}} \left| \left( \hat{Y}_m^I + \hat{Y}_m^Q \right) \cos \phi_l + \left( \hat{Y}_m^Q - \hat{Y}_m^I \right) \sin \phi_l \right| \right] \\ &= \left| \sum_{m=1}^{N^{(1)}} \hat{Y}_m^* P_m^{(\text{ext})} \right| + \left| \sum_{m=N^{(1)}+1}^{N^{(1)}+N} \hat{Y}_m^* P_m^{(\text{ext})} \right| + \left| \sum_{m=N^{(1)}+N+1}^{N^{(\text{ext})}} \hat{Y}_m^* P_m^{(\text{ext})} \right| - \max_l \left[ \sum_{m=1}^{N^{(\text{ext})}} \frac{1}{2} \left| \left( \hat{Y}_m^I - \hat{Y}_m^Q \right) \cos \phi_l + \left( \hat{Y}_m^I + \hat{Y}_m^Q \right) \sin \phi_l \right| + \sum_{m=1}^{N^{(\text{ext})}} \frac{1}{2} \left| \left( \hat{Y}_m^I + \hat{Y}_m^Q \right) \cos \phi_l + \left( \hat{Y}_m^Q - \hat{Y}_m^I \right) \sin \phi_l \right| \right] \\ &= \left| \sum_{m=N^{(1)}+1}^{N^{(1)}+N} \hat{Y}_m^* P_m^{(\text{ext})} \right| - \frac{1}{2} \max_l \left[ \sum_{m=1}^{N^{(\text{ext})}} \left| \left( \hat{Y}_m^I - \hat{Y}_m^Q \right) \cos \phi_l + \left( \hat{Y}_m^I + \hat{Y}_m^Q \right) \sin \phi_l \right| + \sum_{m=1}^{N^{(\text{ext})}} \left| \left( \hat{Y}_m^I + \hat{Y}_m^Q \right) \cos \phi_l + \left( \hat{Y}_m^Q - \hat{Y}_m^I \right) \sin \phi_l \right| \right] \quad (15) \end{aligned}$$



then the accumulation (sum) of the received samples, thus resulting in a complexity of  $2N^{(\text{ext})}$ :

$$\text{Complexity } \Gamma_B^{(\text{ext})} = L_2(\alpha N + 2N^{(\text{ext})}) = 734L_2 \quad (21)$$

where  $L_2$  is the number of iterations required to detect the synchronization sequence for  $\Gamma_B^{(\text{ext})}$ . This solution becomes interesting when complexity or energy consumption is a relevant issue on the receiver side.

#### F. DETECTOR IMPLEMENTATION

Two approaches are possible for the implementation of the detector in Equation (15).

2) Moving window: The statistical test is computed on a moving window shifting by one sample at a time, and directly compared to a threshold. If the threshold is exceeded, the detector stops and outputs the estimated starting point of the pattern. Otherwise, the window is moved forward by one symbol.

3) Block processing: If we work with blocks of symbols in the frequency/time domain, the detector can first identify the statistical value maximum inside the block and then compare it against the threshold. If the threshold is exceeded, the detector stops and outputs the estimated starting point of the pattern. Otherwise, the next non-overlapping block is processed. Given a set of correlation values computed in a certain block of  $S$  subcarriers, the block processing metric  $\Gamma_{BP}$  that is compared with the threshold is

$$\Gamma_{BP} = \max_{s \in [0, \dots, S-N^{(\text{ext})}-1]} \left\{ \Gamma_s^{(\text{ext})} \right\} \quad (22)$$

with  $\Gamma_s$  the result of a generic detection metric for a received sequence of length  $N$  starting at subcarrier  $s \in [0, \dots, S - N^{(\text{ext})} - 1]$  and ending at subcarrier  $s + N^{(\text{ext})} - 1$ .

#### IV. LAND MOBILE SATELLITE CHANNEL MODEL

A review and comparison of different channel models for a variety of satellite communication scenarios can be found in [34]. A popular statistical channel model for satellite communications, named LMS channel, is introduced by ITU in [35], which can be seen as an extension of the model studied by Lutz in [36]. This channel is based on the concept of two-state fading, where the user could be in a good or bad state, depending on the impairments (shadowing) affecting the direct signal, usually referred to as the Line of Sight (LOS) component. The LMS model envisages a variety of environments to characterize different propagation conditions, such as for rural, wooded, urban, and suburban areas, for different satellite elevation angles. In our work, we want to reduce the scenarios to get a general overview of the detector behaviour. Thus, we set the parameters independently from the environment and satellite elevation. Since we are considering handheld devices with limited antenna gains and satellite links with very high path losses, we can reasonably reduce our focus on users in the good state case. The signal is then characterized by the contribution

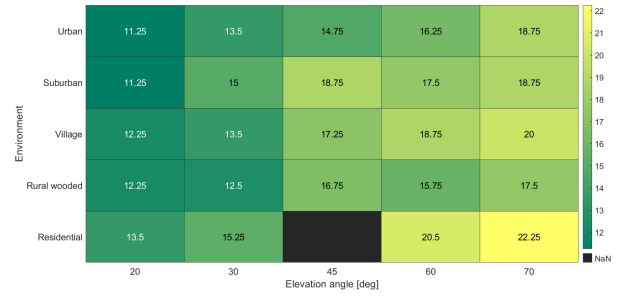


FIGURE 7. Measured K factor values for a confidence interval of 95%, at 2.2 GHz.

of a strong LOS component and the multipath, generated by the nearby scatterers. This kind of signal propagation is modelled in [35] as a Rician Fading channel. The complex multipath component is the fast-varying component of the channel and is characterized by the Doppler Spread resulting from the relative mobile-satellite velocity  $v$ . It is generated via the sum of two Gaussian series  $a \sim \mathcal{N}(0, 1)$ , one for the in-phase and one for the in-quadrature component, and then passed through a unit-energy Doppler filter, based on the Jackes model

$$S(f) = \begin{cases} \frac{G}{\pi f_m \sqrt{1-(f/f_m)^2}} & \text{if } |f| < f_m \\ 0 & \text{otherwise} \end{cases} \quad (23)$$

where  $f_m = v f_c / c$  with  $f_c$  the carrier frequency,  $c$  the speed of light, and  $G$  is a normalization parameter which ensures that the filtering does not change the processing power. Finally, the actual amplitude of the multipath is given by the result of the complex series multiplied with  $\sigma_{MP}$ , being  $2\sigma_{MP}^2$  the mean square value of the multipath variations, and it depends on the Rician  $K$  factor, given by  $K = v^2 / 2\sigma_{MP}^2$ , with  $v^2$  the direct path power. In Figure 7 we reported the  $K$  factors for different elevations and environments with a confidence interval of 95%, from measurements in [35], for frequencies between 1.5 and 3 GHz.

The LMS channel is then time-varying, due to the mobility of the user, and frequency flat, given a negligible delay spread. This last assumption holds in most scenarios for satellite communications, but different kinds of wireless channels could be considered if strong scattered paths with significant delays are present [24]. We leave these cases for future studies.

#### V. SIMULATION RESULTS

In this section we present the simulation results, comparing the new enhanced PSS detector against standard correlation techniques. The main system parameters are reported in Table 3. We first evaluate the technique performance in the AWGN channel with ICI, and then we introduce also the LMS channel.

##### A. DETECTION TECHNIQUES COMPARISON IN PRESENCE OF FO

Before analyzing the specific performance for PSS synchronization, we analyze the performance of different detection

**TABLE 3.** Main system parameters.

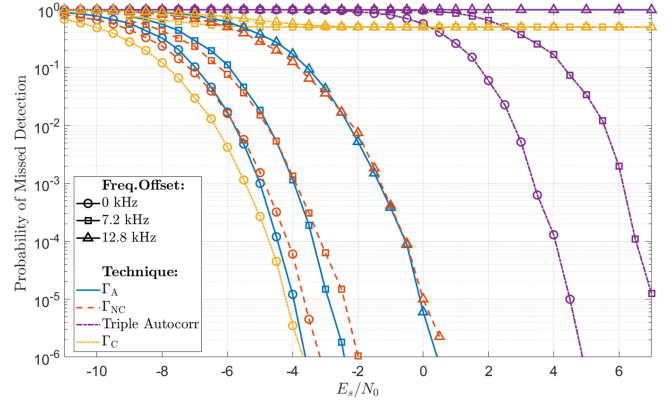
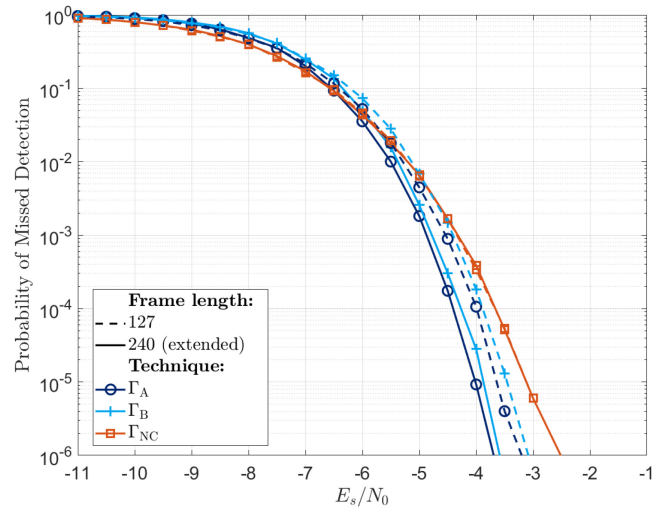
Parameter	Value
Carrier frequency $f_c$	L-Band 1.6 GHz
Numerology $\mu$	1
Subcarrier spacing SCS $\Delta f = 15 \cdot 2^\mu$ kHz	30 kHz
Transmission Time Interval TTI = $1 \cdot 2^{-\mu}$ ms	0.5 ms
SSB Bandwidth $B$	7.20 MHz
FFT dimension per OFDM symbol $N_{\text{FFT}}$	256
Symbol Energy $E_s$	1 J
Antenna Configuration	SISO
Residual Frequency Offset RFO $\psi$	[0, ..., 8] ppm
Data symbols modulation	QPSK
Number of LRT phase shifts $N_q$	4
Rician factor $K$	{10, 20} dB
User speed $v$	5 km/h

techniques in the case of a generic OFDM system, when FO is present and then the samples in the frequency domain are affected by ICI.

We carried out several tests with different levels of FO and  $E_s/N_0$ , with  $N_0$  the noise power spectral density, and we computed the  $\mathcal{P}_{\text{MD}}$ , fixed a desired  $\mathcal{P}_{\text{FA}}$ . The results can be seen in Figure 8, for a  $\mathcal{P}_{\text{FA}} = 10^{-6}$ . When no FO is present, the advantage lies in the coherence detection curve, but the LLR metric  $\Gamma_A$  of Equation (16) starts to approach the same performance as SNR is increased. The non-coherent technique is better only at lower SNR, but in a range of missed detection probability already quite low: in real systems, acceptable values are  $\mathcal{P}_{\text{MD}} < 10^{-2}$ . Coherent detection fails with the introduction of FO into the received signal, as for the curve of 4.5 ppm (parts per million) FO, i.e., 7.2 kHz, due to the additional phase offset which disrupts the coherence with the local sequence. LLR and non-coherent detection experience a moderate loss but are still reliable. This FO value is close to the 3GPP requirement of robustness for an initial 5 ppm CFO due to UE oscillator misalignment. A third case with a FO of 8 ppm, i.e., 12.8 kHz, is also considered. This FO level is particularly harmful since it is approaching half the subcarrier spacing, and it can be seen that all the techniques suffer large losses, and the LLR solution does not provide a clear advantage anymore. Nevertheless, it does not lose much ground against the non-coherent solution. We also implemented a detection technique based on the triple autocorrelation properties described in [10], but it does not perform well in this scenario. We expected this result since this technique is actually designed as a refinement step after non-coherent correlation is performed with down-sampled sequences in the time domain.

### B. 5G NR SSB DETECTION PERFORMANCE WITH THE ENHANCED DETECTOR

The next step is the performance evaluation of the new enhanced detector  $\Gamma_A^{(\text{ext})}$  of Equation (15) analytically derived in the previous section. We will investigate both the moving

**FIGURE 8.** Detection techniques comparison with different FO and  $\mathcal{P}_{\text{FA}} = 10^{-6}$ .**FIGURE 9.** Moving Window,  $\mathcal{P}_{\text{MD}}$  vs.  $E_s/N_0$ . RFO = 160 Hz and  $\mathcal{P}_{\text{FA}} = 10^{-6}$ .

window and block processing approaches, and we will consider different values of SNR and RFO and a random phase offset. The main system parameters are summarized in Table 3.

In our scenario of pre-compensated CFO and Doppler shift, in compliance with 3GPP requirements on the receiver accuracy, the considered RFO is 0.1 ppm [37]. The 5G carrier frequency under analysis is 1.6 GHz, so the inserted RFO is 160 Hz, considerably lower than the FO values considered in the first tests.

1) Moving Window: To analyse the proposed approach we first focus on the application of a moving window and a threshold test.

In Figure 9 we fix a threshold corresponding to a false alarm probability of  $10^{-6}$ , and we plot the behaviour of the missed detection probability. These results show that, by exploiting the PSS structure, and taking into account the extended pattern and the nature of the symbols surrounding it, a significant gain can be achieved. We add as a comparison also the curves resulting from Equation (18), which shows how this approximation still provides good results, and can be a viable lower complexity choice for the detector.

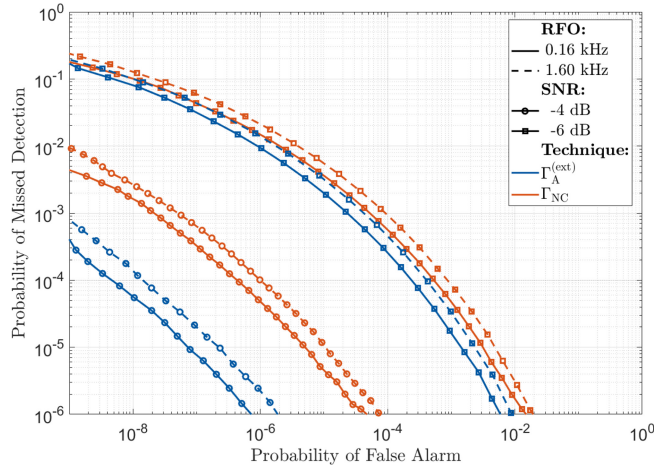


FIGURE 10. Moving window, ROC curves for different  $E_s/N_0$  levels.

In Figure 10 we compare the Receiver Operating Characteristic (ROC) curves in terms of the probability of missed detection vs. the probability of false alarm for the non-coherent and the proposed approaches. The curves are generated with an RFO of 0.1 ppm (160 Hz), but also with an RFO of 1 ppm (1.6 kHz). These results confirm the gain in the detection performance for the entire span of the false alarm probabilities. Moreover, the new technique proves its robustness against possible higher FO.

2) Block processing: Since block processing looks appealing for our scenario, in this section we present additional results referring to this approach, where the test is computed on the entire window, but only the maximum is compared against the threshold. The time/frequency window is the same size as the SSB: 256 subcarriers and 4 OFDM symbols.

The block processing approach allows us to understand the impact of a mixed case, that occurs when the detection window is partially overlapped with the pattern, and that it is not taken into account when the hypothesis testing approach is considered as in the previous case. Its impact is usually considered negligible [20]. Anyway, it can increase the false alarm probability in case the pattern is not well designed or it is too short. When we consider the block processing approach, if the detector maximum is achieved in a position different from the correct one, it generates an error. Thus, the mixed case problem is completely taken into account.

Here we consider detection only over blocks that certainly contain the PSS. In this case, the three possible events are:

- Correct detection when the block maximum is above the threshold and corresponds to the PSS pattern.
- False alarm when the block maximum is above the threshold but not aligned with the PSS pattern.
- Missed detection when the block maximum is below the threshold.

Results are shown in Figure 11, where the gain of the technique is still appreciable for this block processing approach. Note that the false alarm probability is now set also to  $10^{-3}$ : we are dealing with a lower number of test results at a time than the moving window, since only the

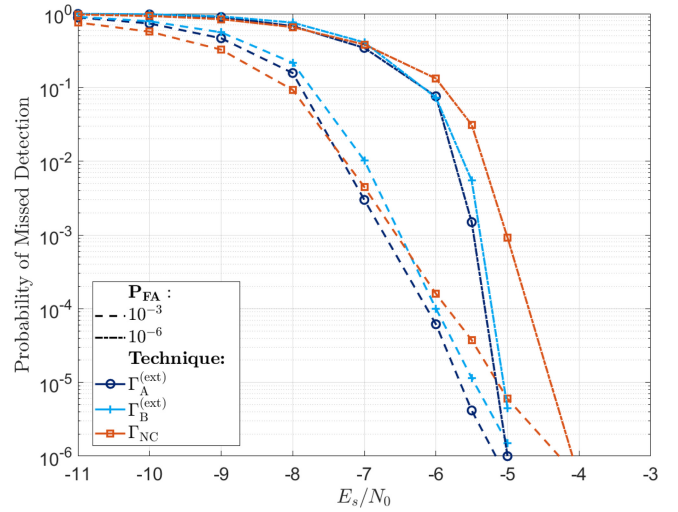


FIGURE 11. Block processing,  $\mathcal{P}_{MD}$  vs.  $E_s/N_0$  and RFO = 160Hz.

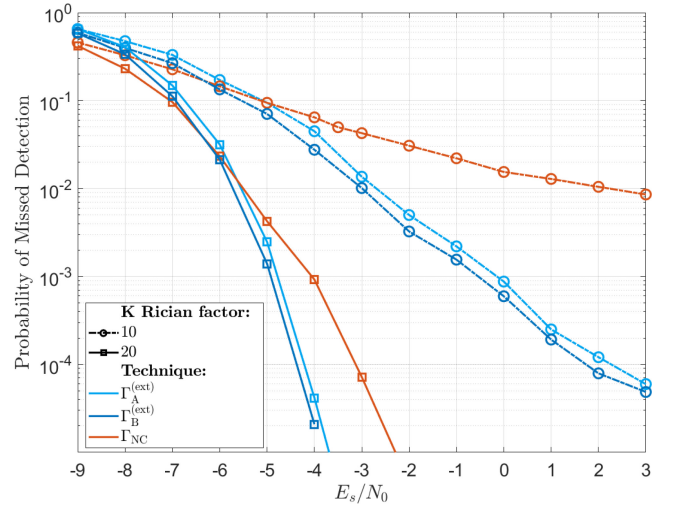


FIGURE 12. Moving Window, LMS channel with user moving at 5 km/h,  $\mathcal{P}_{MD}$  vs.  $E_s/N_0$  and RFO = 160Hz.

maximum test value is compared with the threshold. In other words, a block that produces  $256 \times 4$  test values, which could occur in possibly  $256 \times 4 - 1$  false alarms with the sliding window, can now produce at most one false alarm. Thus, we can accept a higher rate of false positive, higher as a factor approximately the number of samples in the block ( $\approx 10^3$ ).

### C. DETECTOR PERFORMANCE WITH LMS CHANNEL MODEL

After testing the detector with the generic AWGN channel, we investigate its performance when the signal is affected by the LMS channel. We consider the case when users are moving at a walking speed of 5 km/h. For the selection of the Rician  $K$  factor, we can assume that low values of  $K$  represent scenarios where multipath can be quite strong, as in urban environments and low elevation angles of the satellite, while higher values are typical of suburban or rural environments and elevation angles closer to  $90^\circ$ .



[35, Fig. 14] shows the Cumulative Distribution Functions of the  $K$  factor for different environments. From those results and the values we reported in Figure 7, we decided to perform simulations for two extreme values of  $K$ , which are 10 and 20 dB. In Figure 12 are reported the detector results for the LMS channel. The presence of the fading channel can in general degrade the performance of the detection for both techniques, but the advantages of the new detector that exploits the SSB structure increase as the  $K$  factor decreases. This can be explained by the fact that the fading channel is moving the operational point to a higher SNR due to the additional multipath effect, but this permits to better exploit the presence of data on the received signal, given that the noise power in that range is lower. Also in this case, the performance of the approximated technique  $\Gamma_B^{(ext)}$  experience a small loss compared to  $\Gamma_A^{(ext)}$ , and can be an interesting alternative for complexity-constrained receivers.

## VI. CONCLUSION

In this paper we have investigated PSS detection for 5G NTN scenarios, characterized by low SNR values and RFO due to imperfect Doppler compensation that translates into OFDM ICI. We have analytically derived an enhanced detector based on (i) a precise model of ICI effect (ii) the optimal statistical test in case of phase offset and QPSK symbols (iii) an extended pattern encompassing the PSS sequence. Simulation results, including the LMS channel model, show that the enhanced detector is able to outperform traditional non-coherent correlation and is robust under realistic NTN downlink scenarios. The technique, presented for 5G NR under the NTN scenario, can also be applied to other 3GPP technologies that use an SSB with a similar structure, such as NB-IoT and RedCap.

## ACKNOWLEDGMENT

The authors are grateful to Roberto Fantini and Bruno Melis of TIM for useful discussions and suggestions. RICCARDO TUNINATO acknowledges support from TIM through Ph.D. scholarship. The authors are grateful to the reviewers for the helpful suggestions that have allowed to improve the manuscript.

## REFERENCES

- [1] V. Bioglio, C. Condo, and I. Land, "Design of polar codes in 5G new radio," *IEEE Commun. Surveys Tuts.*, vol. 23, no. 1, pp. 29–40, 1st Quart., 2021.
- [2] A. Guidotti et al., "Architectures, standardisation, and procedures for 5G satellite communications: A survey," *Comput. Netw.*, vol. 183, Dec. 2020, Art. no. 107588. [Online]. Available: <https://www.sciencedirect.com/science/article/pii/S138912862031224X>
- [3] S. Won and S. W. Choi, "Three decades of 3GPP target cell search through 3G, 4G, and 5G," *IEEE Access*, vol. 8, pp. 116914–116960, 2020.
- [4] R. Tuninato, D. Riviello, R. Garellò, B. Melis, and R. Fantini, "A comprehensive study on the Synchronization procedure in 5G NR with 3GPP-compliant link-level simulator," *J. Wireless Commun. Netw.*, vol. 2023, no. 111, pp. 1–29, Oct. 2023.
- [5] J.-C. Lin, "Synchronization requirements for 5G: An overview of standards and specifications for cellular networks," *IEEE Veh. Technol. Mag.*, vol. 13, no. 3, pp. 91–99, Sep. 2018.
- [6] J.-L. Yin, M.-C. Lee, W.-H. Hsiao, and C.-C. Huang, "A novel network resolved and mobile assisted cell search method for 5G cellular communication systems," *IEEE Access*, vol. 10, pp. 75331–75342, 2022.
- [7] Y. He, Y. Gu, S. Bu, and Z. Mao, "Primary Synchronization signal design for new radio technique in 5G communication system," in *Proc. 1st Workshop Fog Comput.-Based Radio Access Netw. 5G*, 2017, pp. 265–269.
- [8] K. Ota, A. Shimura, M. Sawahashi, and S. Nagata, "Performance of physical cell ID detection probability considering frequency offset for NR radio interface," in *Proc. IEEE 90th Veh. Technol. Conf. (VTC2019-Fall)*, 2019, pp. 1–6.
- [9] F. Chen, X. Li, Y. Zhang, and Y. Jiang, "Design and implementation of initial cell search in 5G NR systems," *China Commun.*, vol. 17, no. 5, pp. 38–49, 2020.
- [10] D. Wang, Z. Mei, H. Zhang, and H. Li, "A novel PSS timing synchronization algorithm for cell search in 5G NR system," *IEEE Access*, vol. 9, pp. 5870–5880, 2021.
- [11] E. S. Warner, B. Mulgrew, and P. M. Grant, "Triple correlation analysis of binary sequences for codeword detection," *IEE Proc.-Vis. Image Signal Process.*, vol. 141, no. 5, pp. 297–302, 1994.
- [12] A. Omri, M. Shaqfeh, A. Ali, and H. Alnuweiri, "Synchronization procedure in 5G NR systems," *IEEE Access*, vol. 7, pp. 41286–41295, 2019.
- [13] Y.-H. You and H.-K. Song, "Efficient sequential detection of carrier frequency offset and primary synchronization signal for 5G NR systems," *IEEE Trans. Veh. Technol.*, vol. 69, no. 8, pp. 9212–9216, Aug. 2020.
- [14] M. Wang, D. Hu, L. He, and J. Wu, "Deep-learning-based initial access method for millimeter-wave MIMO systems," *IEEE Wireless Commun. Lett.*, vol. 11, no. 5, pp. 1067–1071, May 2022.
- [15] C. Hu and Y. Zhang, "5G NR primary synchronization signal detection with low hardware resource occupancy," in *Proc. IEEE/CIC Int. Conf. Commun. China (ICCC)*, 2018, pp. 304–308.
- [16] N. Cassiau, L. Maret, J.-B. Doré, V. Savin, and D. Kténas, "Assessment of 5G NR physical layer for future satellite networks," in *Proc. IEEE Global Conf. Signal Inf. Process. (GlobalSIP)*, 2018, pp. 1020–1024.
- [17] Y. Liu et al., "The time-frequency Synchronization for 5G NR based non-terrestrial networks," in *Proc. IEEE 21st Int. Conf. Commun. Technol. (ICCT)*, 2021, pp. 587–591.
- [18] "Discussion on DL coverage enhancement for NR NTN," 3GPP, Changsha, China, document TSG-RAN WG1 Meeting #116bis, ZTE R1-2402622, 2024.
- [19] H. Huawei, "Discussion on downlink coverage enhancements for NR NTN," 3GPP, Changsha, China, TSG-RAN WG1 Meeting #116bis, 3GPP R1-2402003, 2024.
- [20] M. Chiani and M. Martini, "On sequential frame Synchronization in AWGN channels," *IEEE Trans. Commun.*, vol. 54, no. 2, pp. 339–348, Feb. 2006.
- [21] M. Chiani, "Noncoherent frame synchronization," *IEEE Trans. Commun.*, vol. 58, no. 5, pp. 1536–1545, May 2010.
- [22] A. Elzanaty, K. Koroleva, S. Gritsutenko, and M. Chiani, "Frame Synchronization for M-ary modulation with phase offsets," in *Proc. IEEE 17th Int. Conf. Ubiquitous Wireless Broadband (ICUWB)*, 2017, pp. 1–6.
- [23] "Technical specification group services and system aspects; release 17 description; summary of Rel-17 work items; (Release 17), Version 17.0.1," 3GPP, Sophia Antipolis, France, Rep. TR 21.917, 2023.
- [24] "Technical specification group radio access network; study on new radio (NR) to support non-terrestrial networks; (Release 15), Version 15.4.0," 3GPP, Sophia Antipolis, France, Rep. TR 38.811, 2020.
- [25] "Technical specification group radio access network; non-terrestrial networks (NTN) L/S-band for NR; (Release 18), Version 18.1.0," 3GPP, Sophia Antipolis, France, Rep. TR 38.741, 2024.
- [26] I. Ali, N. Al-Dhahir, and J. Hershey, "Doppler characterization for LEO satellites," *IEEE Trans. Commun.*, vol. 46, no. 3, pp. 309–313, Mar. 1998.

- [27] E. Dahlman, S. Parkvall, and J. Sköld, "Chapter 16-initial access," in *5G NR: The Next Generation Wireless Access Technology*, E. Dahlman, S. Parkvall, and J. Sköld, Eds. Waltham, MA, USA: Academic Press, 2018, pp. 311–334. [Online]. Available: <https://www.sciencedirect.com/science/article/pii/B9780128143230000168>
- [28] "Physical channels and modulation: (Release 15), Version 15.2.0," 3GPP, Sophia Antipolis, France, Rep. TS 38.211, 2018.
- [29] M. Enescu et al., *5G New Radio: A Beam-based Air Interface-PHY Layer*. Hoboken, NJ, USA: Wiley, 2020, pp. 95–260.
- [30] D. Chandramouli, R. Liebhart, and J. Pirskanen, "Radio access technology," in *5G for the Connected World*, Hoboken, NJ, USA: Wiley, 2019, pp. 51–126.
- [31] P. Moose, "A technique for orthogonal frequency division multiplexing frequency offset correction," *IEEE Trans. Commun.*, vol. 42, no. 10, pp. 2908–2914, Oct. 1994.
- [32] Z. Jie, Z. Yun, S. Ling, and Z. Ping, "Effects of frequency-offset on the performance of OFDM systems," in *Proc. Int. Conf. Commun. Technol. (ICCT)*, 2003, pp. 1029–1032.
- [33] J. Massey, "Optimum frame synchronization," *IEEE Trans. Commun.*, vol. 20, no. 2, pp. 115–119, Apr. 1972.
- [34] V. Monzon Baeza, E. Lagunas, H. Al-Hraishawi, and S. Chatzinotas, "An overview of channel models for NGSO satellites," in *Proc. IEEE 96th Veh. Technol. Conf.*, 2022, pp. 1–6.
- [35] *Propagation Data Required for the Design Systems in the Land Mobile-Satellite Service*, ITU-Rec. P. 681-11, Aug. 2019.
- [36] E. Lutz, D. Cygan, M. Dippold, F. Dolainsky, and W. Papke, "The land mobile satellite communication channel-recording, statistics, and channel model," *IEEE Trans. Veh. Technol.*, vol. 40, no. 2, pp. 375–386, May 1991.
- [37] "User equipment (UE) radio transmission and reception; part-1: Range 1 Standalone; (Release 15), Version 15.2.0," 3GPP, Sophia Antipolis, France, Rep. TS 38.101-1, 2018.



**RICCARDO TUNINATO** (Graduate Student Member, IEEE) received the bachelor's degree in electronic and computer engineering from the Università degli Studi di Trieste in 2018, and the master's degree (cum laude) in communications and computer networks engineering from the Politecnico di Torino in 2020, where he is currently pursuing the Ph.D. degree with the Department of Electronics and Telecommunications Engineering. His main research topic is the study and analysis of the physical layer of communication systems, mainly related to the 5G standard. In particular, he investigated the techniques for synchronization and initial access, and the beamforming techniques for Massive MIMO systems, with the support and collaboration of TIM.



**ROBERTO GARELLO** (Senior Member, IEEE) received the Ph.D. degree in electronic engineering from the Politecnico di Torino in 1994, with a thesis on Error Correction Coding. During his doctorate, he was a visiting student with MIT, Cambridge, and with ETH, Zürich. From 1994 to 1997, he was with Marconi Communications, Genoa. From 1998 to 2001, he was an Associate Professor with the University of Ancona. Since November 2001, he has been an Associate Professor with the Department of Electronics and Telecommunications, Politecnico di Torino. In 2017, he was an Adjunct Professor with California State University, Los Angeles. He has been the Project Manager of 40 research projects, and the advisor of 12 Ph.D. students. His main research topics are space communication systems, 5G and beyond mobile networks, and channel coding. On these topics, he has co-authored more than 150 papers.

Open Access funding provided by 'Politecnico di Torino' within the CRUI CARE Agreement